*buildings*

MDPI

*Article*

# Investigation on the Dynamic Response and Failure Mode of Clay Brick Masonry Walls Under Long-Duration Explosion

**Chengrui Wang, Kai Zhang *, Wei Liu *, Peng Li, Ming Yang and Xiaolei Chen**

State Key Laboratory of Chemistry for NBC Hazards Protection, Beijing 102205, China
* Correspondence: zhangkai@sklnbcpc.cn (K.Z.); lw_email@126.com (W.L.)

**Abstract**

Masonry structures are widely used in civil engineering due to their favorable load-bearing capacity and construction efficiency; however, the threat posed by long-duration blast loads from industrial accidents and large-yield explosions has become increasingly prominent. Existing research has primarily focused on the response of masonry walls under conventional short-duration explosions, while systematic investigations remain limited regarding the differentiated failure mechanisms induced by long-duration blasts. To address this gap, this study adopts and validates a full-scale simplified micro-modeling approach for clay brick masonry walls using LS-DYNA. The model enables systematic comparison of long-duration blast loads and conventional blast loads simulated by the CONWEP method under equal peak overpressure and equal impulse conditions. Numerical results indicate that, under equal peak overpressure (0.18 MPa), the long-duration blast load induces global deformation and cumulative damage leading to complete collapse, whereas the conventional blast load results in only elastic response. Under equal impulse (13.5 kPa·s), both loads cause severe damage, yet the conventional blast load triggers instantaneous localized fragmentation with a higher collapse rate, while the long-duration blast load governs failure through sustained overpressure-induced global deformation and crack propagation. The comparison of mid-span displacement–time histories across different loading cases further quantifies these distinct failure modes, revealing fundamentally different deformation development rates and collapse characteristics. The key contributions of this study are summarized as follows: A validated simplified micro-model is developed that reproduces the experimental damage patterns of masonry walls. A comparison identifies and mechanistically explains the differentiated failure modes between the two load types. Under the conditions considered in this study, critical transition thresholds of peak overpressure and impulse governing the damage mode shift from minor cracking to global collapse are determined. These findings provide a scientific basis for distinguishing blast-resistant design strategies for masonry structures according to explosion type.

**Keywords:** long-duration explosion; clay brick masonry wall; dynamic response; failure mode; numerical simulation

Check for updates

Academic Editor: Mario D'Aniello

Received: 13 April 2026
Revised: 12 May 2026
Accepted: 18 May 2026
Published: 20 May 2026

**Copyright:** © 2026 by the authors. Licensee MDPI, Basel, Switzerland. This article is an open access article distributed under the terms and conditions of the Creative Commons Attribution (CC BY) license.

## 1. Introduction

Masonry structures, owing to their excellent load-bearing capacity, economic efficiency, and ease of construction, have become the dominant structural form in modern civil engineering projects such as residential buildings, office buildings, and commercial centers. According to statistics, over 70% of existing buildings worldwide are masonry structures [1,2]. In recent years, accidents caused by explosions resulting from industrial

or domestic incidents, such as chemical plant explosions or gas leaks in residential areas, as well as terrorist attacks, have occurred frequently across various regions of the world. When subjected to out-of-plane loads generated by explosive impacts, masonry structures may experience cracking, bending, fragmentation, or even progressive collapse [3,4], thereby endangering structural safety, human life, and property. Therefore, investigating the dynamic response of masonry structures under various types of explosive loads is of great significance.

However, current research has primarily focused on the blast resistance and damage mechanisms of masonry structures under low-intensity chemical explosions, while studies on their dynamic response to long-duration explosions remain limited. Keys et al. [5] defined a long-duration explosion as one in which the positive phase duration, the time interval between the arrival of the blast wave and the onset of the negative phase, exceeds 100 milliseconds. Such blast waves can be generated by large-yield trinitrotoluene (TNT) detonations and nuclear explosions. The blast loads induced by long-duration explosions differ fundamentally from those of conventional chemical explosions in key parameters of the pressure-time history, including positive phase duration, peak overpressure, and impulse. Specifically, the considerably extended positive phase duration results in a significantly prolonged period during which the structure is subjected to high pressure, while the peak overpressure is maintained at a relatively high level over a much longer duration. More importantly, due to the combined effects of loading duration and pressure characteristics, the impulse generated by a long-duration explosion far exceeds that of a conventional chemical explosion, exerting a more pronounced sustained loading and cumulative damage effect on the structure. These distinctions lead to markedly different damage mechanisms and protection requirements for building structures. Masonry walls are primarily composed of bricks and mortar, and their overall structural response is governed by the mechanical properties of the constituent materials and the bond strength at their interfaces, exhibiting strong nonlinear characteristics. Owing to their construction method and inherent material brittleness, the dynamic response, damage mechanisms, and debris distribution of masonry structures are closely related to the characteristics of the blast load [6,7].

Research on the blast resistance of masonry structures has primarily employed a combination of experimental testing and numerical simulation. In experimental studies, close-range, small-charge explosion tests are commonly conducted, in which parameters such as reflected overpressure, wall deflection curves, crack distribution, and debris fragmentation are measured to evaluate the blast performance of masonry walls [8,9]. Chiquito et al. [10] conducted blast tests on masonry walls using three different strengthening schemes and assessed the damage degree through multiple parameters to determine damage levels. Their results indicated that strengthening with glass fiber sheets effectively enhanced the blast resistance of brick masonry walls. Yu et al. [11] investigated the failure modes of masonry walls coated with polymer and made of autoclaved aerated concrete (AAC) under chemical explosions. Based on the experimental results, they established a damage evaluation criterion for AAC walls and subsequently developed a cohesive zone model (CZM) using numerical simulation software to replicate the blast tests. The results showed that the polymer coating on the wall surface significantly improved the blast resistance of the masonry, and the CZM was capable of simulating the failure mode of the AAC masonry wall under the tested conditions. Shi et al. [12] conducted field blast tests on 14 clay brick masonry walls to investigate the effects of scaled distance, axial compression ratio, wall thickness, and wall length on the dynamic response and damage patterns of clay brick masonry walls. Key data such as reflected pressure time histories and residual lateral displacements were recorded. The study proposed a five-level damage classifica-

tion system, confirming that increasing the axial compression ratio and wall thickness enhances blast performance, while greater wall length exacerbates damage. These findings provide a critical reference for validating numerical simulations and for the blast-resistant design of load-bearing masonry walls. Li et al. [13] carried out nine full-scale field tests combined with LS-DYNA numerical simulations to explore the effects of distributed and centralized arrangements of carbon fiber reinforced polymer (CFRP) strips on the blast venting resistance of clay brick masonry walls. The results revealed that the centralized arrangement yielded superior strengthening performance, with all walls exhibiting typical flexural failure. After validation against experimental data, parametric analysis using the numerical model indicated that increasing wall thickness and reducing wall height significantly reduced maximum displacement and damage level, and that CFRP offered better strengthening effectiveness than glass fiber reinforced polymer (GFRP) and polyurea during the elastic stage. Varma et al. [14] conducted blast load tests on 27 plain clay brick walls with dimensions of 3 m $\times$ 3 m. The scaled distances employed in the tests were mainly concentrated in the ranges of $1.0 \leq Z \leq 2.0$ m/kg$^{1/3}$ and $2.2 \leq Z \leq 4.4$ m/kg$^{1/3}$. Based on the test results, the relationship between wall damage level and explosive impulse was established, and the effects of wall thickness and boundary conditions on wall response were analyzed.

Given the limitations of chemical explosion tests, such as high costs, significant safety risks, and poor controllability of experimental conditions, numerical simulation has become a primary research trend in this field for reproducing the interaction between blast waves and masonry structures, as well as the ensuing damage and failure processes. Michaloudis et al. [15] conducted numerical modeling to investigate the mechanical response of unreinforced masonry walls under far-field and contact explosion loads, developing differentiated modeling strategies tailored to the characteristics of each load type. For far-field explosions, the load was applied based on empirical formulas, with emphasis on modeling interface failure; for contact explosions, a Eulerian mesh was constructed to explicitly simulate blast wave propagation, enabling accurate capture of local damage and fragmentation in the near-field region. Validated through four numerical cases and experimental data, the model effectively predicted wall deflection, breach size, and debris scattering characteristics, providing a reliable approach for numerical simulation of blast-resistant masonry structures. Mollaei et al. [16] developed a finite element model of autoclaved aerated concrete (AAC) masonry walls using ABAQUS, simulating walls of three different thicknesses subjected to lateral blast loads from 5 kg and 7 kg TNT charges at varying standoff distances. The study investigated stress distribution, displacement response, energy dissipation characteristics, and crack propagation, and analyzed the influence of boundary conditions. The results indicated that AAC masonry walls exhibited poor blast resistance, with damage significantly exacerbated by short standoff distances, small wall thicknesses, and larger charge masses. The study also noted that the dynamic behavior of AAC materials under high strain rates warrants further experimental investigation. Zu et al. [17] investigated the failure characteristics of 370 mm thick masonry walls under contact explosions and the blast mitigation effect of polyurea elastomer coatings through a combined approach of numerical simulation and experimental validation. The study found that 1 kg TNT was the critical charge mass for contact explosions on this wall type; beyond this threshold, crater size growth stagnated, and energy was dissipated through fragment projection and wall deformation. Double-sided polyurea spray coating significantly enhanced blast resistance and restrained debris scattering, with an optimal configuration of 6 mm coating on the blast-facing side and 2 mm on the rear face, offering a practical solution for blast-resistant masonry wall strengthening. Chiquito et al. [18] used LS-DYNA to study the blast performance of unreinforced walls, as well as those strengthened with carbon fiber and

glass fiber reinforced polymers. A detailed micro-modeling approach was employed to characterize the masonry material properties, and the model was validated using pressure, acceleration, and residual displacement metrics. The results showed that the model accurately reproduced the blast response of the walls; although it slightly underestimated plastic displacement in strengthened walls, it proved suitable for various blast scenarios and protective schemes, serving as an effective predictive tool for blast-resistant design of masonry walls. Ji et al. [19] developed a numerical model of a 40 mm thick masonry wall using LS-DYNA to investigate its failure behavior under contact explosions and the blast mitigation effect of polyurea elastomer coatings. The study identified 0.5 kg TNT as the critical charge mass for contact explosions on this wall type; beyond this value, crater size growth slowed, and energy was primarily dissipated through debris projection and wall deformation. A double-sided polyurea spray coating configuration with 6 mm on the blast-facing side and 2–8 mm on the rear face effectively encapsulated debris, absorbed blast energy, and significantly reduced damage on the rear face. Specifically, with an 8 mm thick coating on the rear face, the damaged area was reduced by 55.6% compared to the unstrengthened wall. Numerical simulations were in good agreement with experimental results, providing an effective technical reference for the blast-resistant strengthening of masonry walls.

In recent years, long-duration blast loads, such as those generated by large-yield TNT explosions, industrial accidents, and nuclear explosions, have attracted considerable attention due to their prolonged duration and high impulse, posing a serious threat to masonry walls [20]. Current research on long-duration explosions has primarily focused on the characteristics of the blast source and the propagation behavior of shock waves. Based on existing blast load data, some researchers have derived explicit equations for calculating blast load parameters and developed efficient numerical simulation methods to enable reliable prediction of far-field free-air or surface-burst blast loads [21,22]. Other scholars have established two-dimensional multi-material fluid dynamics models based on Eulerian coordinates, incorporating adaptive mesh refinement techniques to numerically simulate the ground reflection process of intense air blast waves at varying burst heights. This modeling approach effectively captures complex wave structures such as regular reflection and Mach reflection, with computed peak overpressure and impulse showing good agreement with experimental data over a large spatial scale, thereby providing robust support for damage prediction and selection of detonation configurations in intense air blast scenarios [23,24]. Nevertheless, systematic research on the performance of masonry structures under long-duration blast loads remains limited, particularly regarding comparative studies on the differences in dynamic response of masonry walls subjected to long-duration versus short-duration blast loads. Given the inherently heterogeneous and brittle dynamic response characteristics of masonry structures, along with the complex nature of long-duration blast loads, further investigation into the dynamic behavior of masonry structures under such loading conditions is urgently needed.

In this study, a finite element model of a clay brick masonry wall was established and validated based on the experiments reported in reference [12]. The dynamic responses, failure modes, and damage levels of the masonry wall under long-duration blast loads and CONWEP blast loads were compared and analyzed. Furthermore, the effects of peak overpressure, positive phase duration, and impulse of the two types of blast loads on the damage characteristics of the masonry wall were discussed. The findings provide a reference for future research on the blast response of masonry structures subjected to long-duration blast loads.

In this study, a full-scale simplified micro-model of a clay brick masonry wall is established and validated against the experimental results of Shi et al. [12]. Based on this

validated model, the dynamic response and failure modes of the masonry wall under long-duration blast loads are systematically compared with those under conventional blast loads simulated by the CONWEP method. The specific contributions of this work are threefold. First, the validated simplified micro-model reproduces the damage patterns, displacement distributions, and overpressure time histories observed in the field blast tests, providing a reliable numerical tool for comparative analysis. Second, the comparison under equal peak overpressure (0.18 MPa) and equal impulse (13.5 kPa·s) conditions reveals fundamentally different failure mechanisms: under equal peak overpressure, the long-duration blast load causes progressive global deformation and collapse, whereas the CONWEP load induces only elastic response; under equal impulse, the CONWEP load triggers instantaneous localized fragmentation with a higher collapse rate, while the long-duration blast load governs failure through sustained overpressure-induced global deformation and crack propagation. The distinct failure modes are further quantified by comparing the mid-span displacement–time histories across different loading cases. Third, under the conditions considered in this study, the critical transition thresholds of peak overpressure (0.92–2.41 MPa for CONWEP) and impulse (12.2–13.5 kPa·s for long-duration loading) that govern the damage mode shift from minor cracking to global collapse are determined. These contributions distinguish this study from existing LS-DYNA-based blast analyses that predominantly focus on single blast scenarios, and provide a scientific basis for type-specific blast-resistant design of masonry structures.

## 2. Numerical Modeling and Validation

This study conducts numerical simulation analyses using the explicit dynamic finite element software LS-DYNA (V971_R15). A full-scale finite element model of a clay brick masonry (CBM) wall is established based on the blast test described in reference [12], and the validity of the computational model is verified against the experimental results. To ensure that the numerical simulation accurately reproduces the experimental phenomena, the boundary conditions, material constitutive parameters, and blast loading parameters employed in the model are strictly defined in accordance with the experimental setup detailed in reference [12]. Through comparative analysis with the experimental results, the accuracy and reliability of the proposed model in simulating the blast response of masonry walls are validated.

### *2.1. Numerical Model*

Typically, masonry walls are composed of bricks and mortar, two materials with distinct static and dynamic mechanical properties, exhibiting significant anisotropy and heterogeneity. This structural characteristic leads to three main finite element modeling strategies: the macro-homogeneous model, the detailed micro-model, and the simplified micro-model, as illustrated in Figure 1 [25]. The macro-homogeneous model (Figure 1a) treats masonry as a homogeneous continuum, offering the advantages of simple modeling and high computational efficiency, making it suitable for global response analysis of large-scale masonry structures. However, this type of model fails to capture the individual material properties of bricks and mortar or their interfacial behavior, and it struggles to accurately represent localized failure modes in masonry walls. The detailed micro-model (Figure 1b) requires separate modeling of bricks and mortar, enabling a more realistic description of the mesostructure and failure mechanisms of masonry. Nevertheless, because the mortar layer, typically only about 10 mm thick, must be considered, the mesh size is relatively small, leading to a complex modeling process and significantly increased computational cost. To balance accuracy and computational efficiency, the simplified micro-model (Figure 1c) has gained considerable attention in recent years. In

this approach, the brick is extended in the thickness direction to the midline of the mortar layer, effectively integrating the brick and half of the adjacent mortar thickness into a single extended block element. The interfaces between these extended blocks are then modeled using surface-based cohesive contact pairs, which effectively reduces modeling and computational complexity while preserving the capacity to characterize key mechanical behaviors [26].

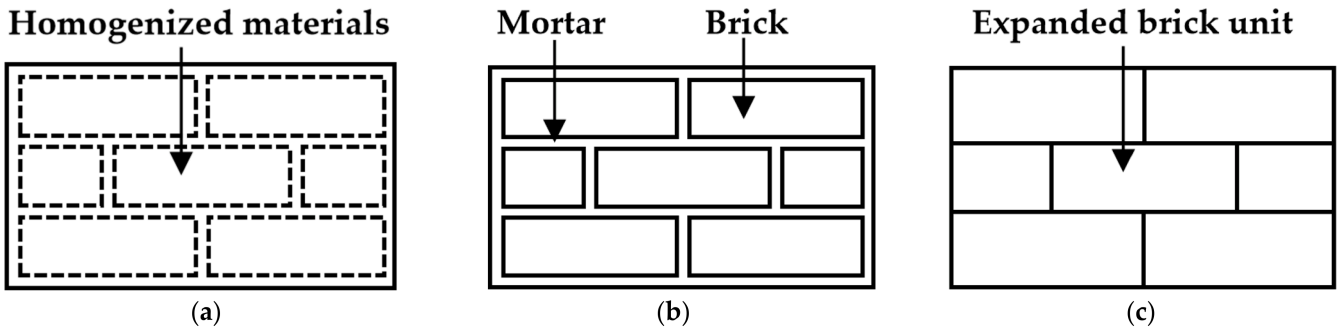



**Figure 1.** Modeling strategies of brick masonry: (**a**) macro-homogeneous model; (**b**) detailed micro-model; (**c**) simplified micro-model.

In this study, a simplified micro-modeling approach is adopted to perform full-scale modeling of the masonry wall used in the experiments, as shown in Figure 2. The wall was constructed in strict accordance with the Code for Design of Masonry Structures (GB 50003-2011) [27] and consists of masonry components and a reinforced concrete (RC) tectonic framework. The wall measures 3.5 m in height and 2.5 m in width, and is built with clay bricks of dimensions 240 mm × 115 mm × 53 mm, with a mortar layer thickness of 10 mm. A steel loading frame with excellent blast load-bearing capacity was installed on the exterior side of the wall, serving both to position the wall and to provide fixed constraints along its top and bottom edges.

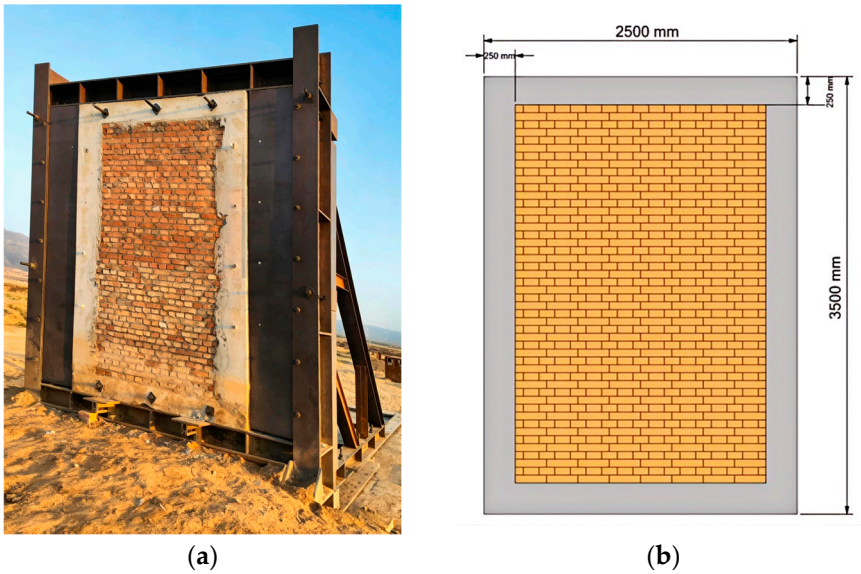



**Figure 2.** (**a**) masonry wall for blast test setup [12]; (**b**) numerical model of masonry wall.

Regarding the mesh discretization, the expanded brick units are modeled with a characteristic element size of 40 mm. This mesh size was selected based on the mesh convergence studies for masonry walls under blast loading conducted by Li et al. [9] and Chiquito et al. [18], who examined three mesh sizes of approximately 10 mm, 20 mm, and

40 mm. Their results showed that the displacement–time histories predicted by all three mesh densities were in good agreement with the experimental measurements, and that the 40 mm mesh achieved sufficiently accurate predictions while substantially reducing the computational time. Considering the balance between computational accuracy and efficiency, the 40 mm mesh size was adopted for the brick units in the present full-scale masonry wall model.

### *2.2. Material Models*

#### 2.2.1. Expanded Brick Units

In this study, the expanded brick units are modeled using Material Model 96 (*MAT_BRITTLE_DAMAGE) in LS-DYNA. This model is an anisotropic brittle damage model originally developed for concrete materials but is also applicable to a variety of brittle materials. The main material parameters for the expanded brick units are summarized in Table 1. Based on regression analysis of experimental data, the elastic modulus of the brick masonry, $E_b$, can be calculated using Equation (1), where $f_1$ represents the compressive strength of the brick [28,29]. The density and compressive strength were obtained from the material mechanical tests reported in the reference experimental study [12], while the remaining parameters were selected based on relevant literature [3,28].

$$E_b = 4467 f_1^{0.22} \quad (1)$$

**Table 1.** Material parameters of expanded brick units [3,12,28].

| Material | Density/ (kg/m$^3$) | Compressive Strength/MPa | Elastic Modulus/MPa | Poisson's Ratio | Bulk Viscosity/ (MPa/s) | Fracture Toughness/(N/m) | Shear Retention Rate |
|---|---|---|---|---|---|---|---|
| Expanded brick unit | 1880 | 15.42 | 8154 | 0.16 | 0.72 | 140 | 0.03 |

It should be noted that in the simplified micro-modeling approach adopted in this study, the expanded brick units were assigned the material properties of the clay brick alone, without applying any homogenization or equivalent property approach to incorporate the mortar. This treatment is consistent with the established methodology of the simplified micro-model [25,26], in which the mechanical contribution of the mortar is represented not through volumetric material homogenization within the expanded units, but through the cohesive contact interfaces defined between them. Specifically, the mortar acts as the bonding layer, whose tensile and shear failure behavior, including crack initiation, propagation, and eventual separation, is captured by the bilinear traction-separation law with the Benzeggagh–Kenane mixed-mode criterion, as detailed in Section 2.3.

#### 2.2.2. Concrete

In the reinforced concrete frame structure, the concrete material is characterized using the Karagozian & Case (K&C) model (*MAT_CONCRETE_DAMAGE_REL3) in LS-DYNA. This model is formulated within the framework of three-invariant failure surface theory, comprising the yield surface, the maximum strength surface, and the residual strength surface, and is capable of comprehensively describing the yielding, hardening, and softening behavior of concrete under dynamic loading [30].

A notable advantage of the K&C model is its automatic parameter generation capability. The user needs to specify only three fundamental physical properties: density, Poisson's ratio, and uniaxial compressive strength. In addition, a length unit conversion factor and a stress unit conversion factor must be provided to ensure unit system consistency between

the user-defined input and the internal imperial-unit-based calibration. Once these input parameters are given, the model's built-in algorithm automatically derives a complete set of mechanical parameters, including the elastic modulus, the three failure surfaces, the damage evolution functions, and the strain-rate enhancement coefficients. This algorithm has been extensively calibrated against a large database of concrete material tests and has been validated in numerous blast and impact simulations [30,31].

In this study, the density and compressive strength of concrete were determined from the material property tests reported in reference [12]. The five user-defined input parameters required for the K&C model in this study are summarized in Table 2.

**Table 2.** Material parameters of concrete.

| Density/(kg/m$^3$) | Poisson's Ratio | Compressive Strength/MPa | Length Unit Conversion Factor | Stress Unit Conversion Factor |
|---|---|---|---|---|
| 2200 | 0.3 | 37.41 | 39.37 | $1.45 \times 10^{-4}$ |

#### 2.2.3. Rebar

The reinforcing steel is modeled using the *MAT_PLASTIC_KINEMATIC elastic–plastic constitutive model. This model supports isotropic, kinematic, and combined hardening behaviors, and incorporates strain rate effects through the Cowper-Symonds constitutive relation. The corresponding expression for the dynamic increase factor (DIF) is given by Equation (2), where $C$ and $P$ are strain rate parameters that characterize the variation in yield stress of the steel with increasing deformation rate. The material parameters for steel reinforcement are summarized in Table 3. The elastic modulus and yield stress of the three steel reinforcement specifications used in the numerical simulation were obtained from experimental data reported in reference [12], while the remaining parameters were selected based on relevant studies [31,32].

$$F_{\mathrm{DIS}} = 1 + \left(\dot{\varepsilon}/C\right)^{1/P}. \tag{2}$$

**Table 3.** Material parameters of rebar.

| Diameter/mm | Density/(kg/m$^3$) | Young's Modulus/GPa | Yield Strength/MPa | Poisson's Ratio | *C* | *P* |
|---|---|---|---|---|---|---|
| 6 | 7850 | 199.5 | 422.20 | 0.3 | 40 | 5 |
| 12 | 7850 | 218.5 | 605.56 | 0.3 | 40 | 5 |
| 14 | 7850 | 205.4 | 576.55 | 0.3 | 40 | 5 |

### *2.3. Interface Contact and Parameters*

In the simplified micro-model, the interfacial bond behavior between expanded brick units is simulated using surface-based cohesive contact based on the bilinear traction-separation law, also referred to as cohesive contact [33]. This contact model is capable of describing the damage and failure processes at the interface under normal (Mode I), tangential (Mode II), and mixed-mode (combination of Modes I and II) loading conditions. Its constitutive relationship consists of a linear hardening stage followed by a linear softening stage. In the initial stage, the interface exhibits linear elastic behavior, and the relationship between stress and displacement can be expressed as follows [34]:

$$\boldsymbol{t} = \begin{Bmatrix} t_{\mathrm{n}} \\ t_{\mathrm{s}} \\ t_{\mathrm{t}} \end{Bmatrix} = \begin{bmatrix} K_{\mathrm{n}} & 0 & 0 \\ 0 & K_{\mathrm{s}} & 0 \\ 0 & 0 & K_{\mathrm{t}} \end{bmatrix} \begin{Bmatrix} \delta_{\mathrm{n}} \\ \delta_{\mathrm{s}} \\ \delta_{\mathrm{t}} \end{Bmatrix} = \mathbf{K}\delta \tag{3}$$

In this expression, $\boldsymbol{t}$ represents the stress vector, comprising the normal stress ($t_n$) and two shear stresses ($t_s$ and $t_t$); **K** denotes the stiffness matrix, which consists of the normal stiffness ($K_n$) and two shear stiffnesses ($K_s$ and $K_t$); and $\delta_n$, $\delta_s$, and $\delta_t$ are the corresponding separation vectors. Once the displacement reaches the failure threshold, the interfacial stress gradually decreases to zero, and the interface behavior degrades to general surface-to-surface contact, capable of transmitting re-contact pressure and shear stress induced by friction. For mixed-mode failure, the damage initiation and evolution are described using the Benzeggagh–Kenane (B—K) criterion. The initial failure displacement $\delta_m^0$ and the final failure displacement $\delta_m^f$ are determined by the following equations [34,35]:

$$\delta_m^0 = \delta_I^0 \delta_{II}^0 \sqrt{\frac{1+\beta^2}{(\delta_{II}^0)^2 + (\beta\delta_I^0)^2}} \tag{4}$$

$$\delta_m^f = \frac{2(1+\beta^2)}{\delta^0(K_N + \beta^2 K_S)} \left[ G_{IC} + (G_{IIC} - G_{IC}) \left( \frac{\beta^2 \times K_S}{K_N + \beta^2 \times K_S} \right)^{|XMU|} \right] \tag{5}$$

where $\delta_I^0$ and $\delta_{II}^0$ are the initial failure displacements for pure Mode I and pure Mode II, respectively; $G_{IC}$ and $G_{IIC}$ represent the fracture energy release rates for Mode I and Mode II, respectively; *XMU* is the mixed-mode interaction parameter in the Benzeggagh–Kenane criterion, typically taken as −2; and $\beta = \delta_{II}/\delta_I$ is the mixed-mode ratio, with $\delta_I = \delta_n$ and $\delta_{II} = \sqrt{\delta_s^2 + \delta_t^2}$.

It should be noted that, in the present simplified micro-model, the cohesive contact interfaces are implemented via the LS-DYNA built-in surface-based cohesive contact algorithm (*CONTACT_AUTOMATIC_SURFACE_TO_SURFACE_TIEBREAK with Option 9), which adopts a penalty-based stiffness formulation [34]. In this formulation, the normal stiffness ($K_n$) and shear stiffnesses ($K_s$ and $K_t$) appearing in Equation (3) are not user-specified input parameters; rather, they are automatically computed by the solver at the beginning of the simulation, based on the bulk modulus and elastic modulus of the adjacent expanded brick elements and the characteristic element size. A contact stiffness scale factor SLSFAC = 0.1 (the LS-DYNA default for penalty-based contacts) was applied globally to all contact pairs. This automatic generation ensures inherent physical consistency between the bulk element stiffness and the cohesive interface stiffness, and avoids introducing unverified user-defined stiffness values that could lead to spurious interface compliance or numerical instability.

The peak tensile and shear stresses (i.e., $T$ and $S$) at the masonry interface were determined based on the study by Chen et al. [25], with the calculation formulas as follows:

$$\mathrm{T} = 0.141\sqrt{f_2} \tag{6}$$

$$\mathrm{S} = 0.25\sqrt{f_2} \tag{7}$$

In the formula, $f_2$ represents the average compressive strength of the mortar. Based on the uniaxial compression test results reported in reference [12], the compressive strength of the mortar is 9.75 MPa, from which the peak normal and shear stresses at the interface can be calculated. The study by Chen et al. [25] indicates that the values of $G_{IC}$ and $G_{IIC}$ can be derived from $T$ and $S$, respectively. In addition, according to the Code for Design of Masonry Structures in China, the static friction coefficient of the masonry interface is taken as 0.7. Given that the dynamic friction coefficient is generally lower than the static friction coefficient, a value of 0.6 is adopted for the dynamic friction coefficient in this study. The complete set of parameters related to cohesive contact is summarized in Table 4.

**Table 4.** Parameters of cohesive contact.

| Tensile Strength/MPa | Shear Strength/MPa | $G_{IC}$/ (MPa·mm) | $G_{IIC}$/ (MPa·mm) | Coefficient of Static Friction | Coefficient of Kinetic Friction |
|---|---|---|---|---|---|
| 0.44 | 0.78 | 0.0147 | 0.0391 | 0.7 | 0.6 |

### *2.4. Blast Load Model*

In the experiment, a 30 kg cylindrical TNT charge was used as the explosive source and placed on a wooden support approximately 1.2 m in height. The initiation system consisted of a pyrotechnic trigger embedded in the center of the charge's upper surface, equipped with an electric detonator. The high temperature and pressure generated by the explosion caused the wooden support to completely disintegrate. The experimental setup is illustrated in Figure 3.



**Figure 3.** Placement of TNT charges [12].

In the blast test reported in reference [12], the free-field overpressure was measured using a piezoelectric pressure sensor mounted on a bracket placed on flat ground at the same standoff distance as the wall, as shown in Figure 4. One free-field overpressure time history was recorded per blast test.



**Figure 4.** Arrangement of free-field pressure sensor [12].

The residual displacements of the masonry wall after each blast test were measured using the construction setting-out method. Nine measurement points were arranged on the rear face of the wall in a regular grid pattern, as shown in Figure 5, with point 5 located at the geometric center of the wall.




(**a**) (**b**)

**Figure 5.** (**a**) Location of measurement points [12]; (**b**) measurement method—construction setting-out [12].

For the numerical simulation of blast loads, the Arbitrary Lagrangian–Eulerian (ALE) method and the CONWEP (Conventional Weapons Effects Program) method are commonly employed. The ALE method requires the modeling of the air domain and the simulation of shock wave propagation, which entails relatively high computational cost. In contrast, the CONWEP method, developed based on extensive blast test data from the U.S. military [36], applies blast loads directly onto structural surfaces, significantly reducing modeling complexity. This method offers high computational efficiency and is particularly suitable for simple scenarios without obstructions that affect wave propagation [37]. Therefore, the CONWEP method is adopted in this study to compute the blast loads. In the CONWEP algorithm, the overpressure time history of the blast shock wave is described using the modified Friedlander equation:

$$P(t) = P_{ref} \times \cos^2\theta + P_{in} \times \left(1 + \cos^2\theta - 2\cos\theta\right) \quad (8)$$

where $P(t)$ is the overpressure actually acting on the structure, $P_{in}$ and $P_{ref}$ are the incident overpressure and reflected overpressure, respectively, and $\theta$ is the angle of incidence. In LS-DYNA, the blast load on the masonry structure can be applied by inputting parameters such as the charge coordinates, TNT equivalent mass, and explosion source type [35].

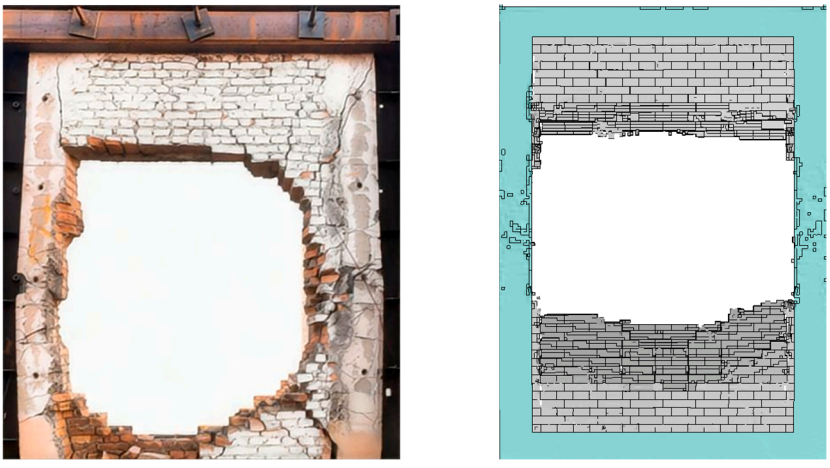
It should be noted that the CONWEP method has several inherent limitations that should be considered when interpreting the simulation results. First, the CONWEP method is based on empirical formulas derived from extensive spherical charge blast tests [36]; it inherently assumes that the blast wave is generated by a spherical charge and propagates isotropically. Consequently, the directional effects produced by non-spherical charges, such as the cylindrical charge used in the reference experiment [12], are not captured. Second, the CONWEP method applies the blast load directly onto the structural surface as a pressure time history and does not explicitly model the propagation of the shock wave through the air or its interaction with surrounding structures. Wave phenomena such as reflection, diffraction, Mach stem formation, and focusing effects caused by structural geometry or ground features are therefore not accounted for. Third, the method is primarily validated for far-field blast scenarios with relatively simple geometries and unobstructed wave propagation paths; its accuracy may degrade for near-field explosions, complex structural configurations, or scenarios with multiple reflecting surfaces.

For applications requiring higher-fidelity blast load predictions, more advanced approaches, such as the Arbitrary Lagrangian–Eulerian (ALE) method with explicit modeling

of the air domain and fluid–structure interaction, can capture the complex wave propagation phenomena that CONWEP cannot resolve. However, ALE simulations entail substantially greater modeling complexity and computational cost. Within the scope of the present study, the CONWEP method is considered adequate because: (i) the experimental scenario involves a relatively simple open-field geometry without obstructions between the charge and the wall; (ii) the charge shape effect on the incident overpressure has been discussed and accounted for in the validation (Section 2.5); and (iii) the parametric analysis focuses on comparing the relative differences in wall response between two loading types under controlled equivalent conditions, for which the CONWEP method provides a consistent and adequate representation of the conventional short-duration blast load.

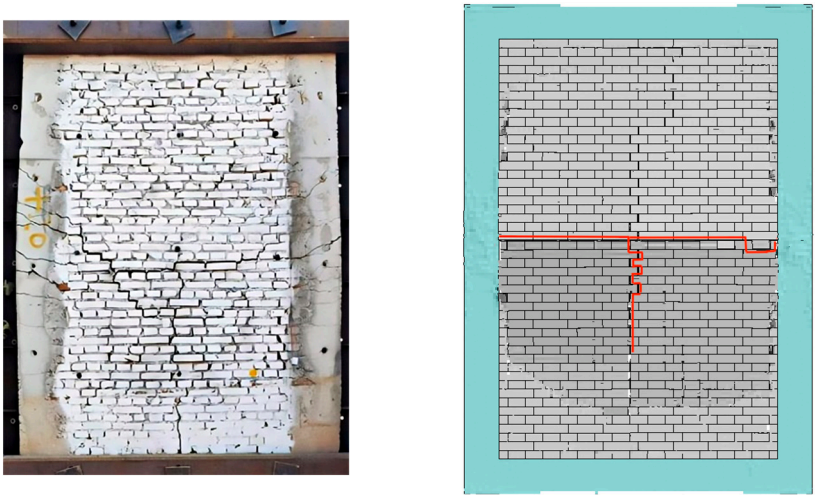
### *2.5. Model Validation*

To validate the numerical model, three test cases from reference [12] with scaled distances of 0.644, 0.965, and 1.287 $m/kg^{1/3}$ were selected for comparison. Figures 6–8 illustrate the damage states of the masonry walls after explosion under the three conditions. As shown in the comparative figures, the numerical simulations successfully reproduced the overall damage patterns of the masonry walls, including flexural-shear deformation, the distribution and propagation paths of cracks (both horizontal and vertical cracks), and captured key damage features such as concrete spalling around the opening and the obvious hole formed under the 30 kg TNT at 2 m standoff condition. The good agreement in both global and local damage morphologies under different blast parameters indicates that the proposed numerical model, with its current material constitutive models and failure criteria, is capable of accurately predicting the complex dynamic response and failure process of masonry walls subjected to blast loads.



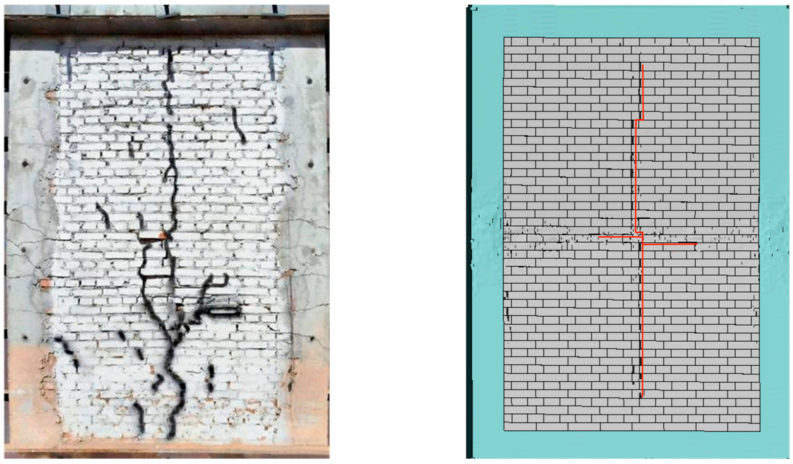
(**a**) (**b**)

**Figure 6.** Overall damage pattern of masonry walls (30 kg & 2 m): (**a**) experimental condition [12]; (**b**) numerical simulation condition.



(**a**) (**b**)

**Figure 7.** Overall damage pattern of masonry walls (30 kg & 3 m): (**a**) experimental condition [12]; (**b**) numerical simulation condition.



(**a**) (**b**)

**Figure 8.** Overall damage pattern of masonry walls (30 kg & 4 m): (**a**) experimental condition [12]; (**b**) numerical simulation condition.

Reference [12] also provides measured incident overpressure data for two test conditions (it should be noted that the incident overpressure was not measured for the 30 kg & 2 m condition). To validate the accuracy of the load input in the numerical simulation, the experimentally measured incident overpressure was compared with the results calculated using the CONWEP method, as shown in Figure 9. The incident overpressure time-history curves obtained from both the experiment and the numerical simulation exhibit a sharp rise followed by an exponential decay, which is consistent with the general characteristics of blast shock waves. The secondary overpressure peak and fluctuations observed in the experimental curves are primarily attributed to the reflected shock waves generated during the expansion of the detonation products and the stability of the test equipment power supply caused by ground vibrations [12,38].

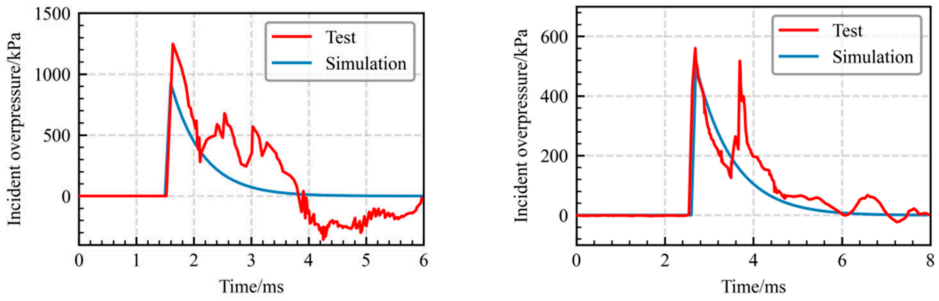



**Figure 9.** Comparison of incident overpressure between numerical predictions and testing data: (**a**) 30 kg & 3 m; (**b**) 30 kg & 4 m.

Under the 30 kg TNT at 3 m standoff condition, the experimentally measured peak incident overpressure was 1250 kPa, while the value calculated using the CONWEP method was 922 kPa, which is 26.24% lower than the experimental value. Under the 30 kg TNT at 4 m standoff condition, the experimentally measured peak overpressure was 560 kPa, and the CONWEP calculated value was 502 kPa, representing a difference of 10.36%. One of the reasons for these discrepancies lies in the charge shape effect. As demonstrated by Shi et al. [39], a cylindrical charge produces greater blast loading in the radial direction than a spherical charge of the same mass, owing to differences in blast wave distribution and directional effects. In contrast, the CONWEP method is based on empirical formulas calibrated from spherical charge detonations, which assume isotropic blast wave propagation. Consequently, for the cylindrical charge employed in the reference experiment [12], the experimentally measured incident overpressures exceed the values predicted by the spherically calibrated CONWEP method.

The experiment also measured the residual displacements at nine points on the surface of the masonry wall, with the locations of the measurement points shown in Figure 5. The residual displacements measured at points 4, 5, and 6 were selected for comparison with the numerical simulation results, as presented in Table 5. Under the 30 kg & 2 m condition, the blast load far exceeded the ultimate resistance of the masonry wall, resulting in a complete loss of load-bearing capacity, and thus the displacements at the measurement points could not be quantitatively measured. Under the 30 kg & 3 m and 30 kg & 4 m conditions, point 5 (located at the center of the wall) exhibited the largest displacement, which aligns with the characteristic that the wall center undergoes the most significant deformation under blast loading. Points 4 and 6, being closer to the edge of the wall, showed relatively smaller displacements. The relative errors were controlled within 25% and 20%, respectively, indicating that the numerical simulation can effectively reproduce the displacement distribution patterns observed in the experiment. Regarding the residual displacement discrepancies, several factors contribute to these differences. First, the simplified micro-modeling approach adopted in this study represents the mortar layer through cohesive contact interfaces rather than modeling it as a separate volumetric material. While this strategy effectively captures crack propagation along the mortar joints, it introduces a slightly stiffer structural response compared to a detailed micro-model, which may result in marginally lower predicted displacements. Second, the blast load input is computed using the CONWEP method, which, as discussed above, underestimates the incident overpressure for the cylindrical charge used in the experiment [12]; a lower input load directly reduces the predicted deformation. Third, for measurement points with small absolute residual displacements (e.g., points 4 and 6 in Table 5, where the measured values are only a few centimeters), the relative error is inherently sensitive to the precision of the construction setting-out measurement technique employed in the reference test [12].

**Table 5.** Comparison of residual displacements.

| TNT Weight/kg | Standoff Distance/m | Scaled Distance/ ($m/kg^{1/3}$) | Displacement Measuring Point | Test Residual Displacement/cm | Simulated Residual Displacement/cm | Relative Error/% |
|---|---|---|---|---|---|---|
| 30 | 2 | 0.644 | 4 | Ejection | Ejection | — |
| | | | 5 | Ejection | Ejection | — |
| | | | 6 | Ejection | Ejection | — |
| 30 | 3 | 0.965 | 4 | 8.0 | 6.1 | 23.75 |
| | | | 5 | 14.9 | 13.6 | 8.72 |
| | | | 6 | 6.2 | 4.7 | 24.19 |
| 30 | 4 | 1.287 | 4 | 7.2 | 5.9 | 18.06 |
| | | | 5 | 10.5 | 8.8 | 16.19 |
| | | | 6 | 4.8 | 4.1 | 14.58 |

Despite these quantitative discrepancies, the model successfully reproduces the essential features of the experimental response: the overall damage morphology (Figures 6–8), the distribution pattern of residual displacements with the maximum at the wall center (Table 5), and the transition of damage modes with varying scaled distance. Moreover, it should be emphasized that the subsequent parametric analyses (Sections 3.2–3.4) compare the response of the same validated model under two different blast loading types (long-duration blast loads vs. CONWEP loads) under controlled equivalent conditions (equal peak overpressure, equal impulse). Consequently, the relative differences in damage patterns and failure mechanisms between the two load types (which constitute the primary contribution of this study) are robust to the absolute accuracy of the displacement predictions. The validation is therefore considered adequate for the objectives of the present study.

It should be noted that the experimental data used for model validation in this study were obtained from the field blast tests conducted by Shi et al. [12]. The validation is therefore limited to the specific experimental configurations reported therein, including the wall geometry, material properties, charge mass, and standoff distances. The inherent uncertainties associated with relying on third-party experimental data, such as the inability to independently verify all test conditions and measurement details, are acknowledged. Nevertheless, the agreement between the numerical predictions and the experimental results in terms of damage patterns, displacement distributions, and overpressure time histories demonstrates that the present model is adequately validated for the objectives of this study.

## 3. Dynamic Response and Damage Characteristics of Masonry Walls Under Long-Duration Blast Loading

In Section 2, the accuracy and reliability of the proposed finite element model of masonry walls in simulating blast loading problems were validated by comparing the numerical simulation results with the chemical explosion test data reported in reference [12]. The adopted material constitutive models, boundary conditions, and contact definitions were shown to effectively capture the dynamic response characteristics of masonry walls. Building upon this validated model, this section first defines the blast load waveform for long-duration explosions employed in the study. Subsequently, a series of comparative cases are designed to systematically evaluate the effects of key parameters, including peak overpressure, positive phase duration, and impulse. Finally, the damage evolution law of masonry walls under long-duration blast loads is elucidated from the perspectives

of damage states and displacement responses. The primary focus is to investigate the differences in failure mechanisms between long-duration blast loads and conventional chemical explosion (short-duration) loads, and to clarify the influence of long-duration blast loading on the failure patterns and mechanical performance of masonry walls.

### *3.1. Definition of Long-Duration Blast Loads*

Significant differences exist in waveform characteristics between long-duration blast waves (such as those generated by far-field nuclear explosions, large-yield TNT detonations, and industrial dust explosions) and conventional chemical explosion waves. The former typically exhibit lower peak overpressure and longer positive phase duration. These differences lead to failure modes and response mechanisms in masonry walls that differ from those induced by conventional explosions. In this study, the defined long-duration blast loads are applied to the blast-facing surface of the clay brick masonry wall model using a surface load application method. During the loading process, the boundary conditions and material parameters of the model are kept consistent with those used in the previous validation phase to ensure the uniqueness of the experimental variable. Only the parameters of the blast load, such as duration and peak overpressure, are varied to ensure that the entire process of the masonry wall under long-duration blast loading (from elastic deformation and plastic damage to cracking and failure) is fully captured.

Varma et al. [14] conducted systematic tests on the blast resistance of ordinary fired brick masonry walls, performing blast tests on a total of 27 specimens measuring 3 m $\times$ 3 m. Based on the final damage states observed in the tests, the damage levels were classified into four grades (A, B, C, and D), arranged in descending order of damage severity. Figure 10 illustrates the final damage morphologies of walls corresponding to the four damage levels. At damage level A, extensive severe deformation occurred over a large area of the wall, with multiple large cracks developing along the peripheral edges of the front face and the central region of the rear face. The displacement at the wall center exhibited a dispersed distribution, accompanied by overall collapse. At damage level B, significant deformation was primarily concentrated in the central portion of the wall, with major cracks forming along the peripheral edges and the central region of the rear face. At damage level C, the wall exhibited slight deformation with only minor cracks. At damage level D, only slight deformation was observed, and the overall structural integrity remained well preserved.

In this study, a total of six overpressure time-history curves were established across three groups. In the first group, the peak overpressure of the long-duration blast load was kept consistent with that of the CONWEP method; in the remaining two groups, the impulse of the two load types was kept consistent. To reasonably determine the values for the equal peak overpressure and equal impulse cases, a critical load analysis was first conducted. For the equal peak overpressure case, the analysis results indicate that when the peak overpressure is below 0.18 MPa, the CONWEP load induces only elastic deformation in the masonry wall, essentially resulting in no visible damage. Under the same peak overpressure level, however, the long-duration blast load leads to overall wall collapse due to its longer duration and larger impulse. To clearly highlight the difference in damage effects between the two load types under identical peak overpressure conditions, a peak overpressure of 0.18 MPa was selected for the equal peak overpressure comparison case. For the equal impulse case, the analysis results show that when the impulse reaches above 12.8 kPa·s, the masonry wall undergoes collapse under the long-duration blast load; when the impulse falls below this value, the wall mainly exhibits minor fragmentation, cracking, and elastic deformation. To systematically investigate the differences in damage mechanisms between the two load types under varying damage levels, two impulse values (13.5 kPa·s and 12.2 kPa·s) were selected as typical cases above and slightly below the

critical value, respectively, to serve as the equal impulse comparison conditions. These values were determined based on preliminary analysis results, ensuring the scientific validity and representativeness of the comparison cases.

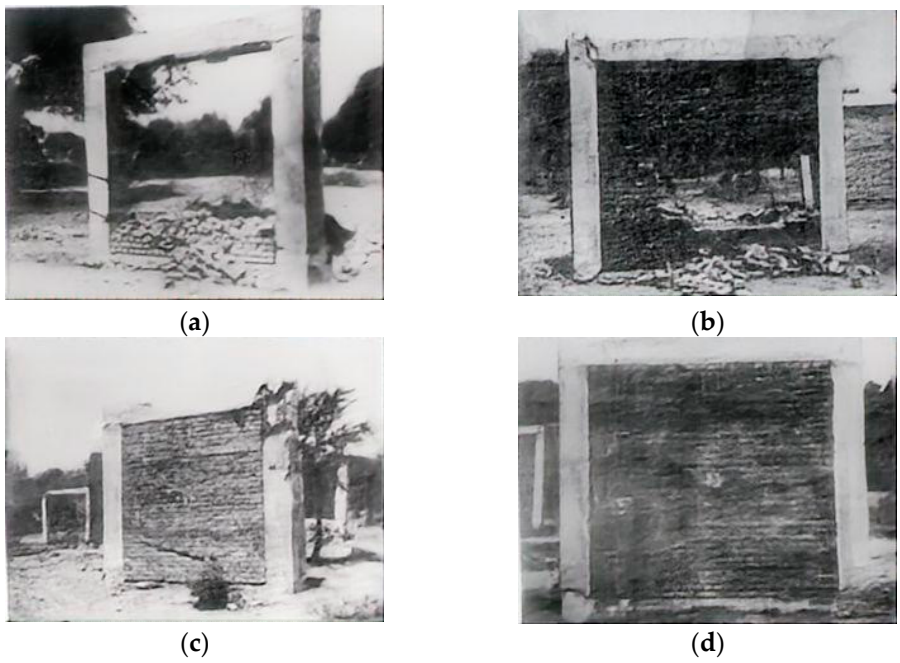


**Figure 10.** Damage levels of masonry walls classified by Varma [14]: (**a**) Level A damage; (**b**) Level B damage; (**c**) Level C damage; (**d**) Level D damage.

### *3.2. Case with Equal Peak Overpressure*

Figure 11a,b shows the CONWEP blast load and the long-duration blast load, respectively, both with an equal peak overpressure of 0.18 MPa.

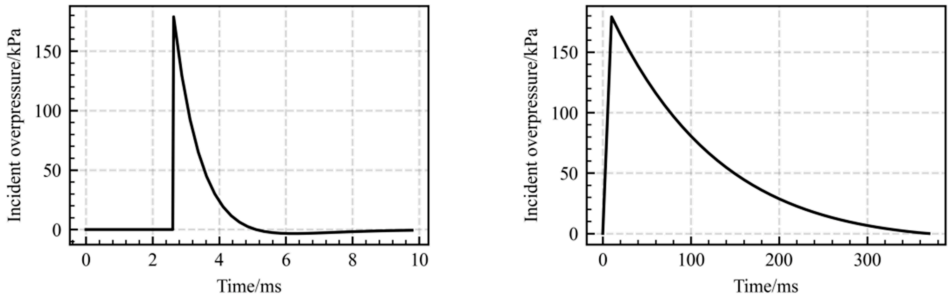
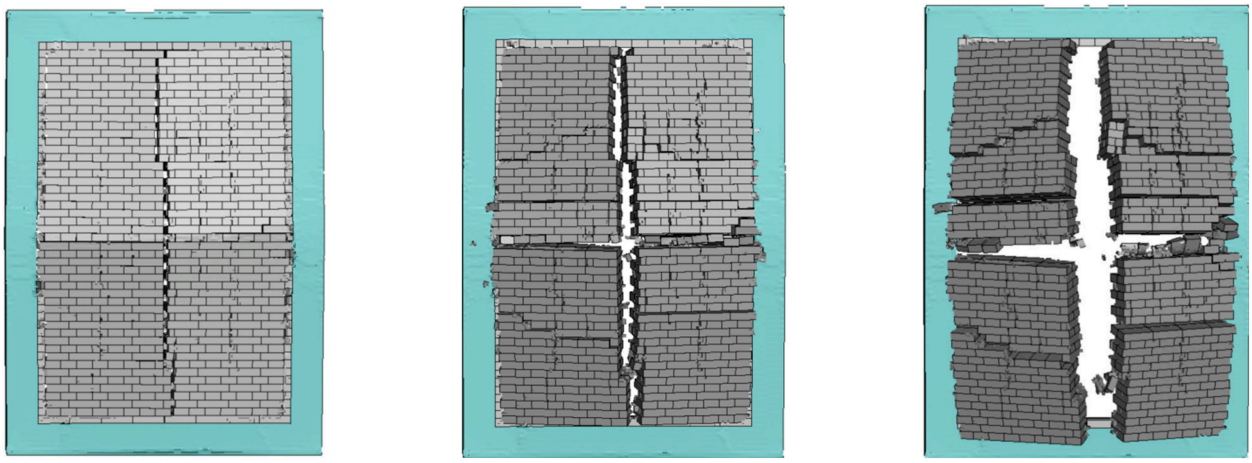



**Figure 11.** Applied blast overpressure time histories: (**a**) CONWEP algorithm; (**b**) long-duration blast loading.

Under identical peak overpressure conditions, the failure modes of the masonry wall subjected to the long-duration blast load differ markedly from those under the equivalent spherical explosive blast load calculated using the CONWEP method. As illustrated in Figure 12, under the long-duration blast load, the wall exhibits pronounced global damage characteristics. Penetrating horizontal and vertical cracks initially appear in the masonry wall, with most cracks propagating along the mortar layer, while cracking and crushing within the clay bricks themselves are relatively scarce. As cracks continue to propagate and coalesce, numerous secondary diagonal cracks develop on both sides of the primary cracks. The bond between masonry units is completely lost, leading to brick sliding, and

the wall enters a stage of large plastic deformation. After the blast load has fully dissipated, the wall undergoes complete through-thickness failure along the primary cracks, splitting into several large independent masonry fragments that disperse, resulting in total collapse, corresponding to damage level A.



(**a**) t = 44 ms (**b**) t = 78 ms (**c**) t = 122 ms

**Figure 12.** Damage to the masonry wall subjected to the long-duration explosion (equal peak overpressure case, 0.18 MPa).

In stark contrast, under the equivalent load calculated using the CONWEP method, the wall exhibits only elastic deformation with minimal displacement response (peak displacement less than 3 mm). Upon dissipation of the load, the wall essentially returns to its original position, with no visible cracks or residual deformation, corresponding to damage level D. The overall displacement contour of the wall is shown in Figure 13. The primary reason for the aforementioned discrepancy lies in the difference in loading duration. The overpressure of the long-duration blast decays slowly. This allows the blast wave to propagate fully within the masonry components, providing sufficient time for the development of global flexural deformation and ultimately leading to overall failure. In contrast, although the equivalent load derived from the CONWEP method shares the same peak overpressure, its positive phase duration is extremely short. The load dissipates before the structure can undergo significant deformation, resulting in only an elastic response without entering the plastic stage.

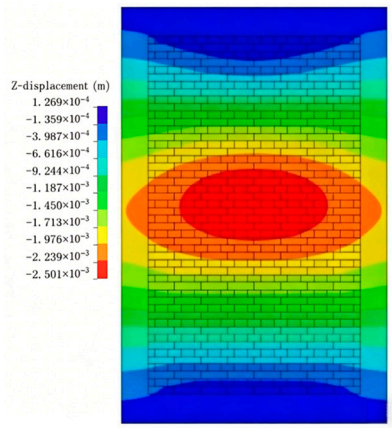



**Figure 13.** Displacement of the masonry wall under CONWEP loading (unit: m).

A direct comparison of the displacement–time histories (Figure 14) reveals the different structural responses under the two loading conditions. Under the CONWEP blast load

(0.18 MPa, impulse 0.12 kPa·s), the wall reaches a peak displacement of less than 3 mm and returns to near its original position, corresponding to damage level D. In contrast, under the long-duration blast load with the identical peak overpressure (0.18 MPa, impulse 18.11 kPa·s), the mid-span displacement increases continuously with progressive plastic deformation, ultimately leading to complete collapse, corresponding to damage level A. This quantitatively confirms that under identical peak overpressure conditions (0.18 MPa), the loading duration and impulse play an important role in governing the structural damage of masonry walls.

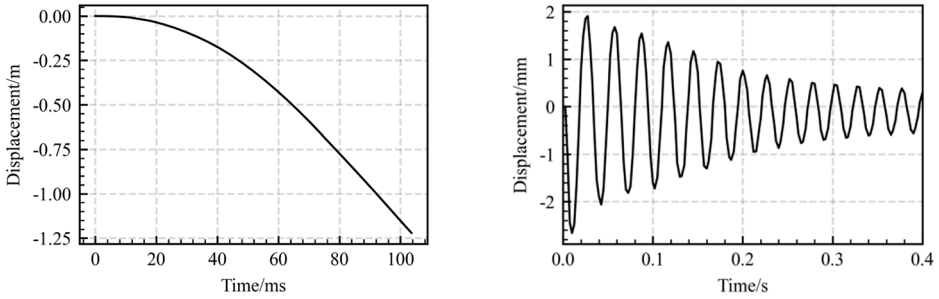



**Figure 14.** Displacement–time history of the mid-span point: (**a**) long-duration explosion; (**b**) CONWEP loading.

### *3.3. Cases with Equal Impulse*

#### 3.3.1. Case 1

Figure 15a,b shows the time-history curves of the blast loads obtained using the CONWEP method and the long-duration blast load, respectively, under equal impulse conditions (approximately 13.5 kPa·s). The impulses of the two cases are 13.49 kPa·s and 13.60 kPa·s, respectively, with a relative difference of less than 1%, allowing them to be treated as equivalent impulse cases.

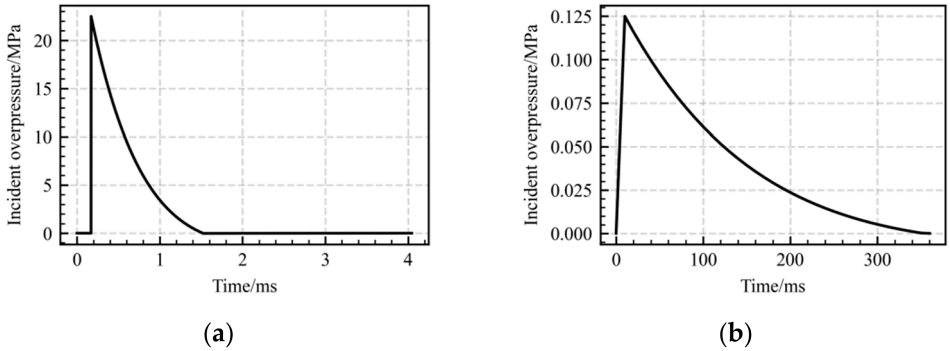
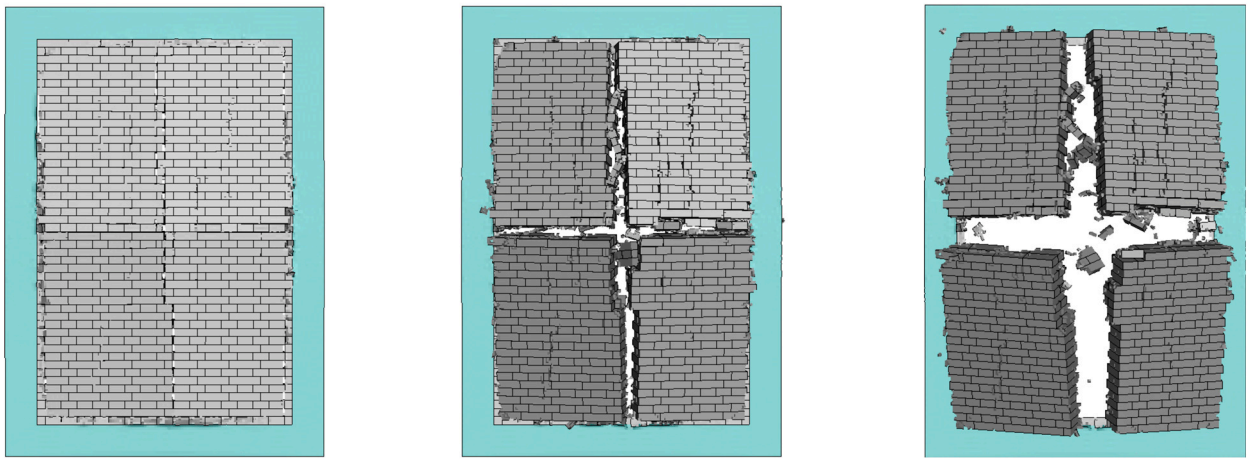



**Figure 15.** Applied blast overpressure time histories: (**a**) CONWEP algorithm; (**b**) long-duration blast loading.

Under both blast loading conditions, the masonry wall undergoes overall collapse failure, and the damage level can be classified as Grade A. However, the failure modes exhibit significant differences between the two conditions, with the core discrepancies stemming from differences in load duration, peak overpressure, and energy propagation characteristics. Under the long-duration blast loading condition, the damage to the masonry wall exhibits a progressive development characteristic, as shown in Figure 16. In the initial stage of loading, initial damage first appears on the blast-facing surface in the form of horizontal and vertical cracks. As the load continues to act, the initial damage gradually develops into visible cracks that continuously propagate. Due to the relatively

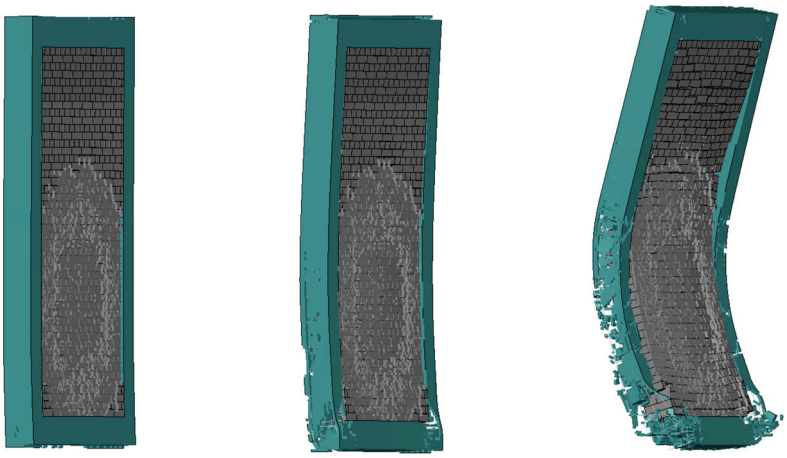
low peak overpressure under this condition, the expanded brick units and reinforced concrete (RC) frame units do not undergo extensive failure. Meanwhile, the overpressure of the long-duration blast decays slowly over time, allowing the blast wave energy to fully propagate and dissipate within the wall. The cohesive contact interfaces at the mortar joints between masonry units do not experience complete failure, with only localized bond damage occurring in the crack propagation areas. The resulting debris consists primarily of small fragments concentrated around the crack zones, with no large-scale projection. Ultimately, the wall undergoes overall splitting due to the through-propagation of major cracks, dividing into four large fragments of comparable size, resulting in a relatively regular overall collapse pattern.



(**a**) t = 49 ms (**b**) t = 136 ms (**c**) t = 186 ms

**Figure 16.** Damage to the masonry wall subjected to the long-duration explosion (equal impulse case 1, 13.5 kPa·s).

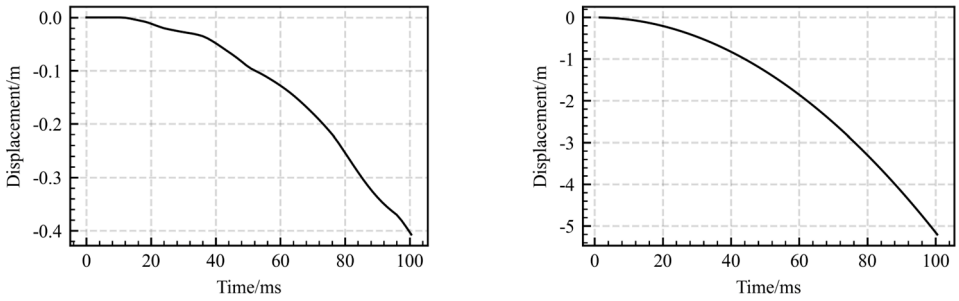
As shown in Figure 17, under the conventional blast loading condition simulated by the CONWEP method, the failure of the masonry wall is characterized by sudden fragmentation and significant flexural deformation. Upon the impact of the blast wave on the blast-facing surface of the wall, energy is highly concentrated in the surface layer of block elements. Owing to the significantly higher peak overpressure under this condition, the block elements on the blast-facing surface rapidly reach the material failure threshold, resulting in element deletion and the immediate appearance of numerous dense cracks on the wall surface. For the RC frame, influenced by the mechanical characteristic that the tensile strength of concrete is much lower than its compressive strength, the degree of concrete failure in the tension zone on the rear face of the frame is significantly higher than that in the compression zone on the blast-facing face, manifesting as obvious tensile cracking and spalling. Under the sustained impact of the high-energy blast wave, a large number of bricks in the wall undergo fragmentation, sliding, and detachment, ultimately leading to overall collapse due to substantial weakening of the effective load-bearing cross-section. After collapse, the wall disintegrates into numerous irregular small fragments with a wider distribution range, exhibiting a more scattered failure morphology.



(**a**) t = 3 ms (**b**) t = 8 ms (**c**) t = 33 ms

**Figure 17.** Damage to the masonry wall subjected to CONWEP loading (equal impulse case 1, 13.5 kPa·s).

The displacement–time history comparison (Figure 18) further quantifies the distinct temporal development of deformation under equal impulse conditions. Both loading cases result in complete wall collapse. However, the collapse rates differ markedly. Under the CONWEP blast load, the mid-span displacement reaches approximately 5 m by 100 ms, indicating rapid and violent collapse (Figure 18b). Under the long-duration blast load, the displacement reaches approximately 0.4 m over the same period, reflecting a slower but progressive collapse process (Figure 18a). Although both loads ultimately result in wall ejection (Grade A), the distinctly different displacement magnitudes and collapse rates quantitatively confirm the different failure mechanisms: instantaneous brittle failure driven by high peak overpressure under short-duration loading (CONWEP blast load) versus progressive damage accumulation driven by sustained overpressure under long-duration loading.

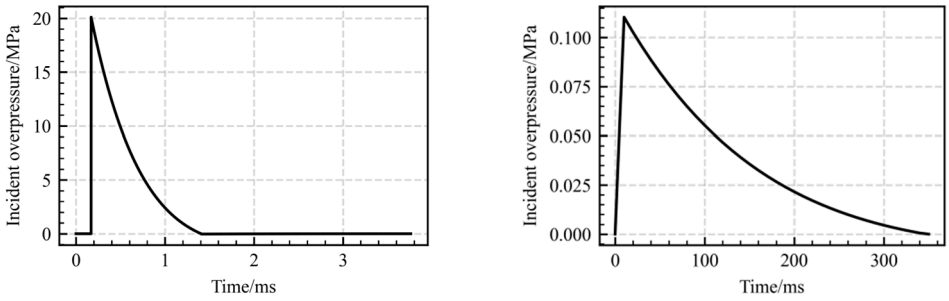



(**a**) (**b**)

**Figure 18.** Displacement–time history of the mid-span point: (**a**) long-duration explosion; (**b**) CONWEP loading.

### 3.3.2. Case 2

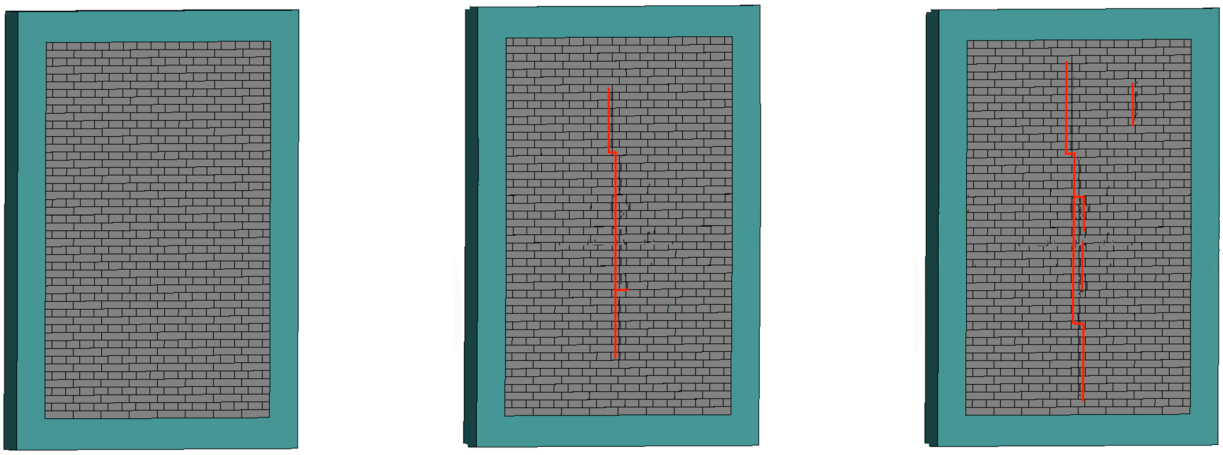
Figure 19a,b shows the time-history curves of the blast loads obtained using the CONWEP method and the long-duration blast load, respectively, under equal impulse conditions (approximately 12.2 kPa·s). The impulses of the two cases are 12.15 kPa·s and 12.20 kPa·s, respectively, with a relative difference of less than 1%, allowing them to be treated as equivalent impulse cases.




(**a**) (**b**)

**Figure 19.** Applied blast overpressure time histories: (**a**) CONWEP algorithm; (**b**) long-duration blast loading.

Figure 20 illustrates the overall damage characteristics of the masonry wall under the long-duration blast load. Under this condition, the dynamic response of the wall is dominated by elastic deformation. Only a small number of expanded brick units undergo element deletion due to the stress reaching the failure threshold, and vertical cracks form in the weak regions of the wall. No severe damage phenomena such as crack penetration, block sliding, or debris projection are observed. Overall, the wall exhibits relatively minor damage without significant loss of structural integrity. The damage level is comprehensively classified as Grade C.

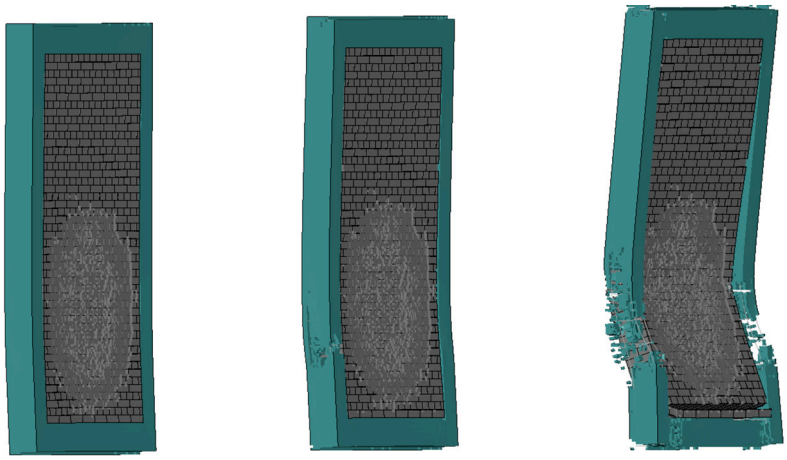


(**a**) t = 2 ms (**b**) t = 33 ms (**c**) t = 132 ms

**Figure 20.** Damage to the masonry wall subjected to the long-duration explosion (equal impulse case 2, 12.2 kPa·s).

As shown in Figure 21, under the blast load simulated by the CONWEP method, the masonry wall exhibits significant flexural deformation, block fragmentation, and overall collapse. The damage characteristics are markedly different from those observed under the long-duration blast load, and the damage level is classified as Grade A. The distribution characteristics of the deleted expanded brick units clearly reflect the propagation characteristics of the spherical blast wave simulated by the CONWEP load, resulting in a damage distribution pattern in the masonry wall that progressively intensifies from the central region outward, with the center of the blast-facing surface being the most severely damaged area. Under the intense action of the high-peak overpressure blast wave, a large number of dense cracks rapidly initiate and propagate across the wall surface. In the key regions of the frame where the blast wave exerts a significant effect, extensive failure and deletion of RC frame elements occur, leaving the internal reinforcing steel completely exposed due to spalling of the concrete cover. The effective load-bearing capacity of the wall is rapidly lost,

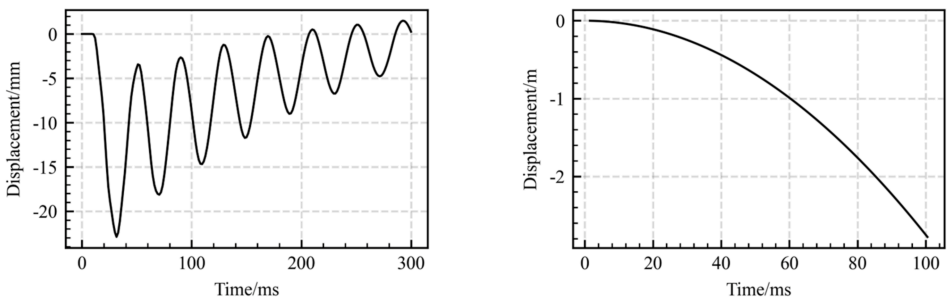
ultimately leading to overall collapse. The overall damage extent is far more severe than that under the long-duration blast loading condition.



(**a**) t =4 ms (**b**) t = 11 ms (**c**) t = 35 ms

**Figure 21.** Damage to the masonry wall subjected to CONWEP loading (equal impulse case 2, 12.2 kPa·s).

Figure 22 illustrates the distinctly different displacement responses under the two loading conditions. Under the long-duration blast load, the maximum mid-span displacement reaches only approximately 23 mm, and the wall response is dominated by elastic deformation with no collapse, corresponding to damage level C (Figure 22a). In contrast, the CONWEP blast load causes complete wall collapse within 100 ms, corresponding to damage level A (Figure 22b). This indicates that when the impulse is held constant at 12.2 kPa·s, the damage level caused by the long-duration blast load is lower than that caused by the CONWEP load. In this case, the peak overpressure of the long-duration blast load is only 0.11 MPa, and despite its positive phase duration exceeding 300 ms, it still fails to cause severe damage to the masonry wall.




(**a**) (**b**)

**Figure 22.** Displacement–time history of the mid-span point: (**a**) long-duration explosion; (**b**) CONWEP loading.

### *3.4. Parametric Analysis*

The blast parameters of the calculated cases in this study are listed in Table 6. It can be concluded that significant differences exist in the failure modes of masonry walls subjected to long-duration blast loads versus loads calculated using the CONWEP method. The conventional blast loads simulated by the CONWEP method are characterized by high peak overpressure and short duration, with the overpressure reaching its peak within an extremely short time followed by rapid decay. The energy is highly concentrated in the central region of the blast-facing surface, resulting in brittle failure such as sudden

fragmentation and localized spalling under instantaneous impact. For the CONWEP method, when the peak overpressure is below 0.92 MPa, the masonry wall primarily exhibits minor damage characterized by cracking or elastic deformation. When the peak overpressure reaches a value between 0.92 and 2.41 MPa, the failure mode of the masonry wall transitions from minor deformation to global deformation and collapse. In contrast, long-duration explosions are characterized by low peak overpressure, long positive phase duration, and large impulse, with the damage dominated by impulse. Under sustained long-duration pressure, the structure undergoes global flexural deformation and cumulative damage, which can cause severe failure even at very low peak overpressure. For the long-duration blast load, when the impulse is below 12.2 kPa·s, the masonry wall mainly exhibits cracking or elastic deformation; when the impulse increases beyond 12.2 kPa·s to 13.5 kPa·s, the failure mode transitions to global deformation and collapse.

**Table 6.** Summary of blast load parameters and structural response for all numerical simulation cases.

| Group | Case | Type of Loading | Peak Incident Overpressure/MPa | Duration/ms | Impulse/kPa·s | Residual Displacement of Mid-Span Point/cm | Damage Levels |
|---|---|---|---|---|---|---|---|
| Explosion test conditions [12] | 1 | CONWEP | 2.41 | 1.97 | 0.52 | Ejection | B |
| | 2 | | 0.92 | 5.64 | 0.51 | 13.60 | C |
| | 3 | | 0.50 | 5.43 | 0.41 | 8.80 | C |
| Equal Peak Overpressure (0.18 MPa) | 4 | Long-duration | 0.18 | 370.50 | 18.11 | Ejection | A |
| | 5 | CONWEP | 0.18 | 2.47 | 0.12 | 0.27 | D |
| Equal Impulse (13.5 kPa·s) | 6 | Long-duration | 0.125 | 361.20 | 13.60 | Ejection | A |
| | 7 | CONWEP | 22.50 | 1.35 | 13.49 | Ejection | A |
| Equal Impulse (12.2 kPa·s) | 8 | Long-duration | 0.11 | 352.30 | 12.20 | 0.12 | C |
| | 9 | CONWEP | 20.12 | 1.23 | 12.15 | Ejection | A |

Note: "Ejection" indicates that the mid-span point could not be measured due to complete wall collapse and fragment ejection. Cases 1–3 correspond to the explosion test conditions in the reference experiment [12] used for model validation. Cases 4–5, 6–7, and 8–9 represent the equal peak overpressure (0.18 MPa), equal impulse (13.5 kPa·s), and equal impulse (12.2 kPa·s) comparison groups, respectively.

Under identical peak overpressure conditions (0.18 MPa), the impulse generated by the long-duration explosion is significantly larger than that of the CONWEP load, resulting in a considerably higher damage level of the wall (Grade A vs. Grade D). This indicates that when the peak overpressure is the same, the positive phase duration and impulse play a decisive role in structural damage. Under equal impulse conditions (13.5 kPa·s), both types of loads cause severe damage, yet their failure modes are fundamentally different: the CONWEP load relies on an extremely high peak overpressure to induce instantaneous localized fragmentation, whereas the long-duration explosion leads to global deformation through sustained overpressure. Notably, when the impulse is kept at 12.2 kPa·s, the damage level caused by the long-duration explosion is lower than that of the CONWEP load. In this case, the peak overpressure of the long-duration explosion is only 0.11 MPa, and despite its positive phase duration exceeding 300 ms, it still fails to cause severe damage to the masonry wall. This further reveals that, under equal impulse conditions, there exists a threshold of peak overpressure that serves as a key indicator governing the damage effect on clay brick masonry walls.

## 4. Conclusions

In this study, a full-scale finite element model of a clay brick masonry wall was established, and numerical simulations of the dynamic response and damage evolution of the masonry wall under blast loads were conducted using a simplified micro-modeling approach within the explicit dynamic analysis software LS-DYNA (V971_R15). The accuracy and reliability of the proposed model in terms of material constitutive laws, interfacial contact, and boundary conditions were validated through comparisons with experimental results, including damage patterns, residual displacements, and incident overpressure time histories. Based on this validated model, the dynamic responses and damage characteristics of masonry walls subjected to long-duration blast loads and conventional blast loads simulated by the CONWEP method were systematically compared. A case with equal peak overpressure and two cases with equal impulse were designed to investigate the effects of peak overpressure, positive phase duration, and impulse on the failure modes of masonry walls. The main findings are as follows:

(1) The simplified micro-scale finite element model developed in this study accurately reproduces the damage patterns, displacement responses, and overpressure time histories of masonry walls under blast loading, confirming the reliability of the material constitutive models, interfacial contact definitions, and boundary condition settings, thereby providing an effective tool for subsequent comparative analyses.

(2) The failure modes of clay brick masonry walls under long-duration blast loads and those simulated by the CONWEP method differ significantly. Under the conditions considered in this study, the long-duration blast load induces overall wall deformation and progressive crack propagation through sustained overpressure, ultimately leading to collapse with a relatively regular failure pattern. In contrast, the CONWEP load, characterized by high peak overpressure, causes instantaneous localized fragmentation and material failure on the blast-facing masonry units, resulting in a more scattered failure pattern.

(3) The damage mechanisms of masonry walls under long-duration blast loads and the CONWEP method differ fundamentally: the former primarily relies on the cumulative damage effects associated with prolonged duration and high impulse, whereas the latter mainly depends on the impact of high peak overpressure. Under the conditions considered in this study, for the CONWEP method, masonry walls primarily exhibit minor damage characterized by cracking or elastic deformation when the peak overpressure is below 0.92 MPa. When the peak overpressure reaches a value between 0.92 and 2.41 MPa, the failure mode of the masonry wall transitions from minor deformation to global deformation and collapse. For long-duration blast loads, when the impulse is below 12.2 kPa·s, the masonry wall primarily exhibits cracking or elastic deformation; when the impulse increases beyond 12.2 kPa·s to 13.5 kPa·s, the failure mode transitions to global deformation and collapse.

(4) In the blast-resistant design of masonry structures, peak overpressure should not be used as the sole evaluation criterion; the assessment should be tailored to the explosion type. Short-duration blasts require attention to local resistance against brittle failure, while long-duration blasts necessitate consideration of crack propagation and impulse accumulation on structural integrity. For brittle components such as masonry walls, the failure modes and corresponding design strategies under the two load types should be clearly distinguished.

**Author Contributions:** Conceptualization, C.W., W.L. and K.Z.; methodology, K.Z., W.L. and P.L.; software, C.W.; validation, C.W. and K.Z.; formal analysis, C.W.; resources, W.L. and P.L.; data curation, C.W., M.Y. and X.C.; writing—original draft preparation, C.W.; writing—review and editing, W.L. and K.Z.; supervision, P.L. and M.Y.; project administration, W.L. and X.C. All authors have read and agreed to the published version of the manuscript.

**Funding:** This research received no external funding.

**Data Availability Statement:** Data are contained within the article.

**Acknowledgments:** The authors gratefully acknowledge Yanchao Shi and the research team at Tianjin University for their kind permission to use the experimental data and figures published in Reference [12] for model validation and comparative analysis in this study.

**Conflicts of Interest:** The authors declare no conflicts of interest.

## References

1. Ettouney, M.; DiMaggio, P.; Hapij, A. Analysis of masonry bearing walls to blast threats. In Proceedings of the Structures Congress, Seattle, WA, USA, 31–29 May 2003.
2. Shi, Y.; Wang, N.; Li, Z.X.; Ding, Y. Experimental studies on the dynamic compressive and tensile strength of clay brick under high strain rates. *Constr. Build. Mater.* **2021**, *272*, 121908. [CrossRef]
3. Zhang, Y.; Hu, J.; Zhao, W.; Hu, F.; Yu, X. Numerical Study on the Dynamic Behaviors of Masonry Wall under Far-Range Explosions. *Buildings* **2023**, *13*, 443. [CrossRef]
4. Thango, S.G.; Drosopoulos, G.A.; Motsa, S.M.; Stavroulakis, G.E. Prediction of the Response of Masonry Walls under Blast Loading Using Artificial Neural Networks. *Infrastructures* **2024**, *9*, 5. [CrossRef]
5. Keys, R.A.; Clubley, S.K. Experimental analysis of debris distribution of masonry panels subjected to long duration blast loading. *Eng. Struct.* **2017**, *130*, 229–241. [CrossRef]
6. Godio, M.; Portal, N.W.; Flansbjer, M.; Magnusson, J.; Byggnevi, M. Experimental and numerical approaches to investigate the out-of-plane response of unreinforced masonry walls subjected to free far-field blasts. *Eng. Struct.* **2021**, *239*, 112328. [CrossRef]
7. D'Altri, A.M.; Sarhosis, V.; Milani, G.; Rots, J.; Miranda, S.D. Modeling Strategies for the Computational Analysis of Unreinforced Masonry Structures: Review and Classification. *Arch. Comput. Methods Eng.* **2020**, *27*, 1153–1185. [CrossRef]
8. Shi, Y.; Xiong, W.; Li, Z.X.; Xu, Q. Experimental studies on the local damage and fragments of unreinforced masonry walls under close-in explosions. *Int. J. Impact Eng.* **2016**, *90*, 122–131. [CrossRef]
9. Li, Z.; Chen, L.; Fang, Q.; Hao, H.; Zhang, Y.; Xiang, H.; Chen, W.; Yang, S.; Bao, Q. Experimental and numerical study of unreinforced clay brick masonry walls subjected to vented gas explosions. *Int. J. Impact Eng.* **2017**, *104*, 107–126. [CrossRef]
10. Chiquito, M.; López, L.M.; Castedo, R.; Pérez-Caldentey, A.; Santos, A.P. Behaviour of retrofitted masonry walls subjected to blast loading: Damage assessment. *Eng. Struct.* **2019**, *201*, 109805. [CrossRef]
11. Yu, Q.; Zeng, D.; Xu, X.; Li, S.; Dong, W.; Dai, L. Experimental and numerical investigation of polymer-reinforced and normal autoclaved aerated concrete masonry walls under large TNT explosive loads. *Int. J. Impact Eng.* **2022**, *164*, 104188. [CrossRef]
12. Shi, Y.; Pan, Y.; Gao, J.; Zhong, W.; Cui, J. Experimental study of the dynamic performance of clay brick masonry walls under blast loading. *Eng. Struct.* **2025**, *343*, 121114. [CrossRef]
13. Li, Z.; Chen, L.; Fang, Q.; Chen, W.; Hao, H.; Zhu, R.; Zheng, K. Experimental and Numerical Study on CFRP Strip Strengthened Clay Brick Masonry Walls Subjected to Vented Gas Explosions. *Int. J. Impact Eng.* **2019**, *129*, 66–79. [CrossRef]
14. Varma, R.K.; Tomar, C.P.S.; Parkash, S.; Sethi, V.S. Damage to brick masonry panel walls under high explosive detonations. *Asme-Publ.-Pvp* **1996**, *351*, 207–216.
15. Michaloudis, G.; Gebbeken, N. Modeling masonry walls under far-field and contact detonations. *Int. J. Impact Eng.* **2019**, *123*, 84–97. [CrossRef]
16. Mollaei, S.; Babaei Ghazijahani, R.; Noroozinejad Farsangi, E.; Jahani, D. Investigation of Behavior of Masonry Walls Constructed with Autoclaved Aerated Concrete Blocks under Blast Loading. *Appl. Sci.* **2022**, *12*, 8725. [CrossRef]
17. Zu, X.; Chen, T.; Cai, Y.; Huang, Z.; Xiao, Q. Blast Resistance of a Masonry Wall Coated with a Polyurea Elastomer. *Coatings* **2022**, *12*, 1744. [CrossRef]
18. Chiquito, M.; Castedo, R.; Santos, A.P.; López, L.M.; Caldentey, A.P. Numerical modelling and experimental validation of the behaviour of brick masonry walls subjected to blast loading. *Int. J. Impact Eng.* **2021**, *148*, 103760. [CrossRef]
19. Ji, L.; Wang, P.; Cai, Y.; Shang, W.; Zu, X. Blast Resistance of 240 mm Building Wall Coated with Polyurea Elastomer. *Materials* **2022**, *15*, 850. [CrossRef] [PubMed]
20. Shi, Y.; Pan, Y.; Wang, S.; Zhong, W.; Cui, J. Damage assessment method of clay brick masonry load-bearing walls under intense explosions with long duration. *Eng. Fail. Anal.* **2024**, *166*, 108830. [CrossRef]
21. Ding, Y.; Zhang, X.; Shi, Y.; Zhang, H. Prediction of far-field blast loads from large TNT-equivalent explosives on gabled frames. *J. Constr. Steel Res.* **2022**, *190*, 107120. [CrossRef]
22. Zhang, X.; Ding, Y.; Shi, Y. Numerical simulation of far-field blast loads arising from large TNT equivalent explosives. *J. Loss Prev. Process Ind.* **2021**, *70*, 104432. [CrossRef]

23. Yao, C.; Wang, H.; Pu, X.; Shou, L.; Wang, Z. Numerical simulation of intense blast wave reflected on rigid ground. *Explos. Shock Waves* **2019**, *39*, 112201. [CrossRef]
24. Yao, C.; Li, R.; Tian, Z.; Guo, Y. Two dimensional simulation for shock wave produced by strong explosion in free air. *Explos. Shock Waves* **2015**, *35*, 585–590. [CrossRef]
25. Chen, D.; Wu, H.; Fang, Q. Simplified micro-model for brick masonry walls under out-of-plane quasi-static and blast loadings. *Int. J. Impact Eng.* **2023**, *174*, 104529. [CrossRef]
26. Zeng, B.; Li, Y.; Noguez, C.C. Modeling and parameter importance investigation for simulating in-plane and out-of-plane behaviors of un-reinforced masonry walls. *Eng. Struct.* **2021**, *248*, 113233. [CrossRef]
27. *GB 50003-2011*; Code for Design of Masonry Structures. General Administration of Quality Supervision, Inspection and Quarantine of the People's Republic of China: Beijing, China, 2011.
28. Riddington, J.R.; Ghazali, M.Z. Hypothesis for shear failure in masonry joints. *Proc. Inst. Civ. Eng.* **1990**, *89*, 89–102. [CrossRef]
29. Atkinson, R.H.; Amadei, B.P.; Saeb, S.; Sture, S. Response of masonry bed joints in direct shear. *J. Struct. Eng.* **1989**, *115*, 2276–2296. [CrossRef]
30. Su, Q.; Wu, H.; Fang, Q. Calibration of KCC model for UHPC under impact and blast loadings. *Cem. Concr. Compos.* **2022**, *127*, 104401. [CrossRef]
31. Su, Q.; Wu, H.; Sun, H.; Fang, Q. Experimental and numerical studies on dynamic behavior of reinforced UHPC panel under medium-range explosions. *Int. J. Impact Eng.* **2021**, *148*, 103761. [CrossRef]
32. Zhang, X.; Hao, H.; Li, C. Experimental investigation of the response of precast segmental columns subjected to impact loading. *Int. J. Impact Eng.* **2016**, *95*, 105–124. [CrossRef]
33. Camanho, P.P.; Davila, C.G. *Mixed-Mode Decohesion Finite Elements for the Simulation of Delamination in Composite Materials*; NASA/TM-2002-211737; NASA: Washington, DC, USA, 2002.
34. Benzeggagh, M.L.; Kenane, M. Measurement of mixed-mode delamination fracture toughness of unidirectional glass/epoxy composites with mixed-mode bending apparatus. *Compos. Sci. Technol.* **1996**, *56*, 439–449. [CrossRef]
35. Livermore Software Technology Gorporation. *LS-DYNA Keyword User's Manual*; Livermore Software Technology Corporation (LSTC): Livermore, CA, USA, 2014.
36. *UFC 3-340-02*; Unified Facilities Criteria (UFC): Structures to Resist the Effects of Accidental Explosions. Department of Defense: Washington, DC, USA, 2008.
37. Nian, X.Z.; Xie, Q.M.; Huang, K. Experimental and numerical study on protective effect of RC blast wall against air shock wave. *Def. Technol.* **2024**, *31*, 567–579. [CrossRef]
38. He, Y.; Chen, L.; Fang, Q.; Xiang, H. Blast loading model of the RC column under close-in explosion induced by the double-end-initiation explosive cylinder. *Eng. Struct.* **2018**, *175*, 304–321. [CrossRef]
39. Shi, Y.; Wang, N.; Cui, J.; Li, C.; Zhang, X. Experimental and numerical investigation of charge shape effect on blast load induced by near-field explosions. *Process Saf. Environ. Prot.* **2022**, *165*, 266–277. [CrossRef]


**Disclaimer/Publisher's Note:** The statements, opinions and data contained in all publications are solely those of the individual author(s) and contributor(s) and not of MDPI and/or the editor(s). MDPI and/or the editor(s) disclaim responsibility for any injury to people or property resulting from any ideas, methods, instructions or products referred to in the content.